Supplementary Information (SI) for RSC Applied Interfaces.

Supplementary Information

Interfacial, solvent-free room-temperature adsorption of quinone derivatives on activated carbon for sustainable energy storage electrodes

Hiroyuki Itoi,[*, a] Ryoma Ito,[a] Manato Matsuo,[a] Yusuke Higashi,[a] Hayato Suzuki,[a] Ginga Saeki,[a] Takafumi Ishii,[b] and Yoshimi Ohzawa[a]*

[a] Department of Applied Chemistry, Faculty of Engineering, Aichi Institute of Technology, 1247 Yachigusa, Yakusa, Toyota, Aichi, 470−0392, Japan

[b] Graduate School of Science and Technology, Gunma University, Kiryu, Gunma, 376-8515, Japan

* Corresponding author E-mail: itoi-hiroyuki@aitech.ac.jp

S1. Effect of adsorption temperature and particle size of TMBQ

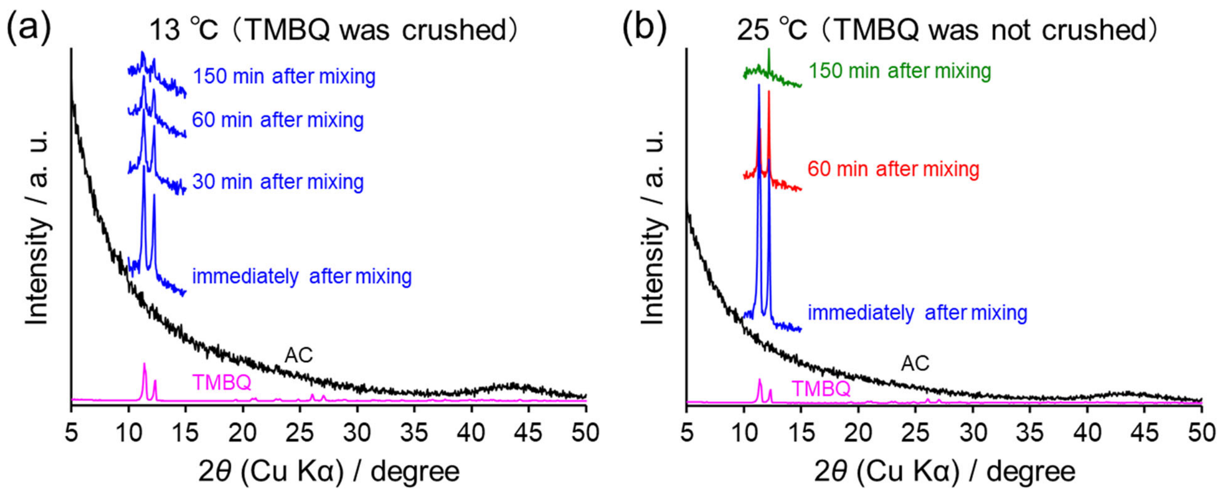

Fig. S1 XRD patterns of AC, TMBQ, and mixtures of AC and TMBQ with 3 mmol of TMBQ per gram of AC. (a) Collected at 13 °C with crushed TMBQ. (b) Collected at 25 °C with uncrushed (as-received) TMBQ.

The XRD patterns shown in Fig. 2 were collected at 25 °C using QDs that had been crushed in a mortar. In contrast, the XRD patterns in Fig. S1a were obtained using crushed TMBQ at 13 °C, whereas those in Fig. S1b were obtained using non-crushed TMBQ at 25 °C. As shown in Fig. S1a and b, the adsorption rate decreased when the temperature was lowed or the particle size of TMBQ was increased.

S2. XRD patterns of AC, QDs, and mixtures of AC and QDs with 6 mmol g^{-1} loading

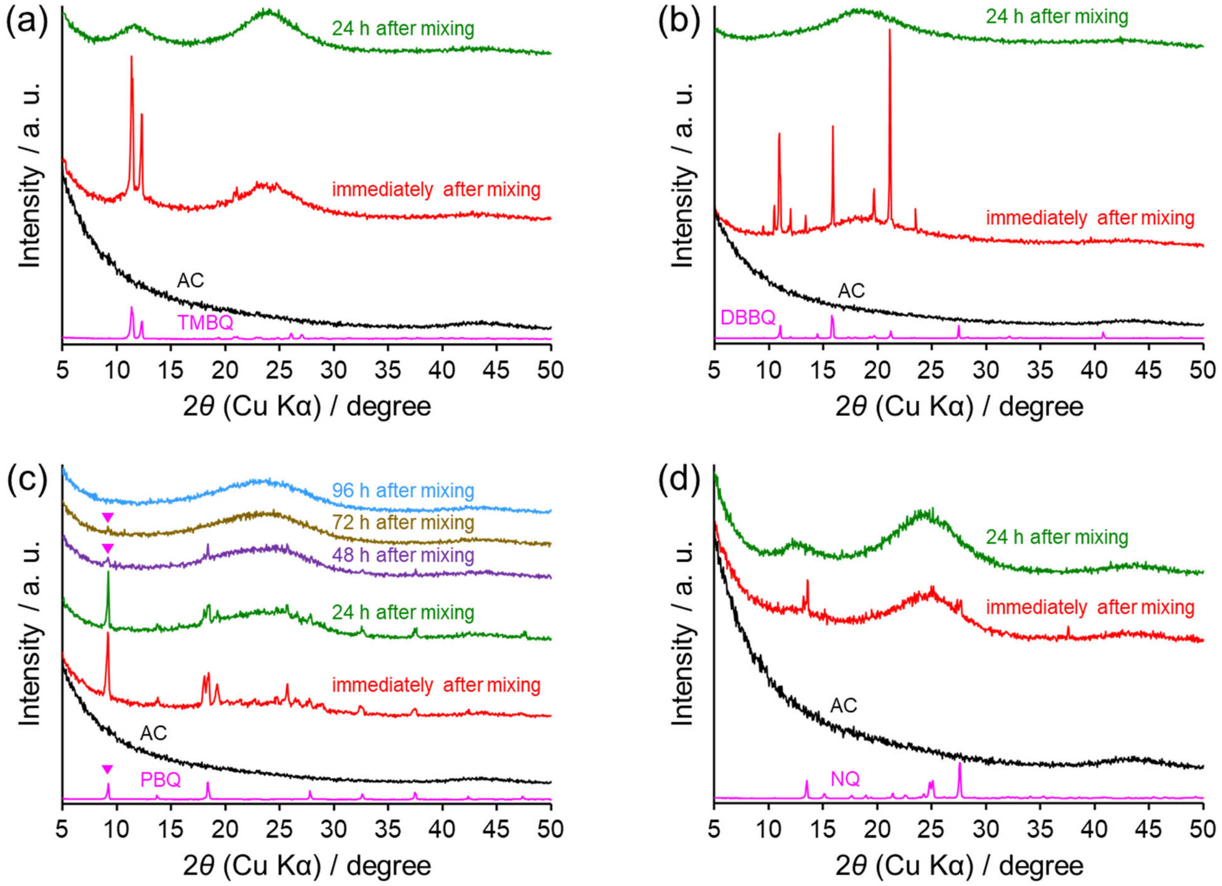

Fig. S2 XRD patterns of AC, QDs, and mixtures of AC and QDs with 6 mmol of each QD per gram of AC. QDs: (a) TMBQ, (b) DBBQ, (c) PBQ, and (d) NQ.

When 6 mmol of QDs were used per gram of AC, the adsorption required a longer period compared with that observed for 2 mmol of QDs per gram of AC (Fig. 2). Specifically, the adsorption of NQ proceeded more slowly than that of the other QDs, showing the same trend as in Fig. 2.

S3. Influence of mixing conditions and container geometry on the adsorption of PBQ onto activated carbon.

To examine the influence of mixing conditions on the adsorption behavior, additional experiments were conducted using PBQ, which exhibits the slowest adsorption among the quinone derivatives and therefore allows clearer evaluation of experimental parameters. In these experiments, the adsorption conditions were standardized to 3 mmol of PBQ per gram of AC, and approximately 100 mg of AC was used.

First, the mixing time using the planetary centrifugal mixer was increased from the original 1 min (2000 rpm) to 3 min and 10 min using a 10 mL glass vial (Fig. S3a). In all cases, adsorption was completed within 48 h, indicating that the mixing time within this range does not significantly influence the overall adsorption process.

Second, the influence of container geometry was examined by replacing the 10 mL glass vial used in the main manuscript with a 24 mL ointment jar and a 13.5 mL screw-cap vial. In both cases, adsorption was also completed within 48 h (Fig. S3a), indicating that the container geometry does not significantly affect the adsorption behavior.

Third, the mixing method was evaluated by manually shaking the mixture, using a tube rotator, or using a roller mixer (Fig. S3b). In these experiments, the number of mixing cycles was adjusted to 2000 to match the total mixing cycles of the planetary centrifugal mixer. Manual shaking resulted in complete adsorption within 48 h, whereas adsorption required up to 72 h when using the tube rotator or roller mixer. This difference is attributed to the slower and less homogeneous mixing in these devices, which makes it more difficult to achieve uniform contact between PBQ and AC particles.

These results indicate that efficient adsorption mainly requires sufficient and homogeneous mixing between the QD crystals and AC particles, whereas the precise mixing time and container geometry have only minor influence under the present experimental conditions.

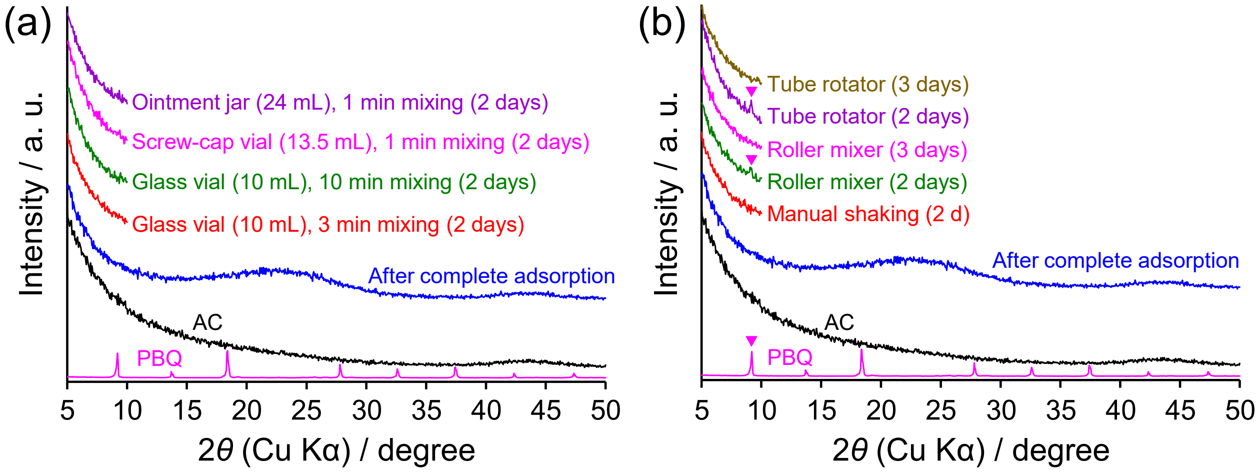

Fig. S3 XRD patterns of AC-PBQ mixtures (3 mmol PBQ per gram of AC) obtained under different mixing conditions. The labels “2 days” and “3 days” in the legends indicate the time after mixing at which the samples were measured. (a) Mixing performed using a planetary centrifugal mixer (ARE-310, THINKY) at 2000 rpm. The mixing time and container geometry were varied (e.g., 1–10 min; 10 mL glass vial, 24 mL ointment jar, and 13.5 mL screw-cap vial). In all cases, PBQ adsorption was completed within 2 days. (b) Mixing method dependence at a fixed total of 2000 mixing cycles. The mixtures were prepared by manual shaking (in a 13.5 mL screw-cap vial), tube rotator, (in a 10 mL glass vial) or roller mixer (in a 13.5 mL screw-cap vial), and the XRD patterns were recorded 2 and/or 3 days after mixing to evaluate the adsorption progress.

S4. Adsorption of TMBQ and DBBQ onto AC via the indirect method

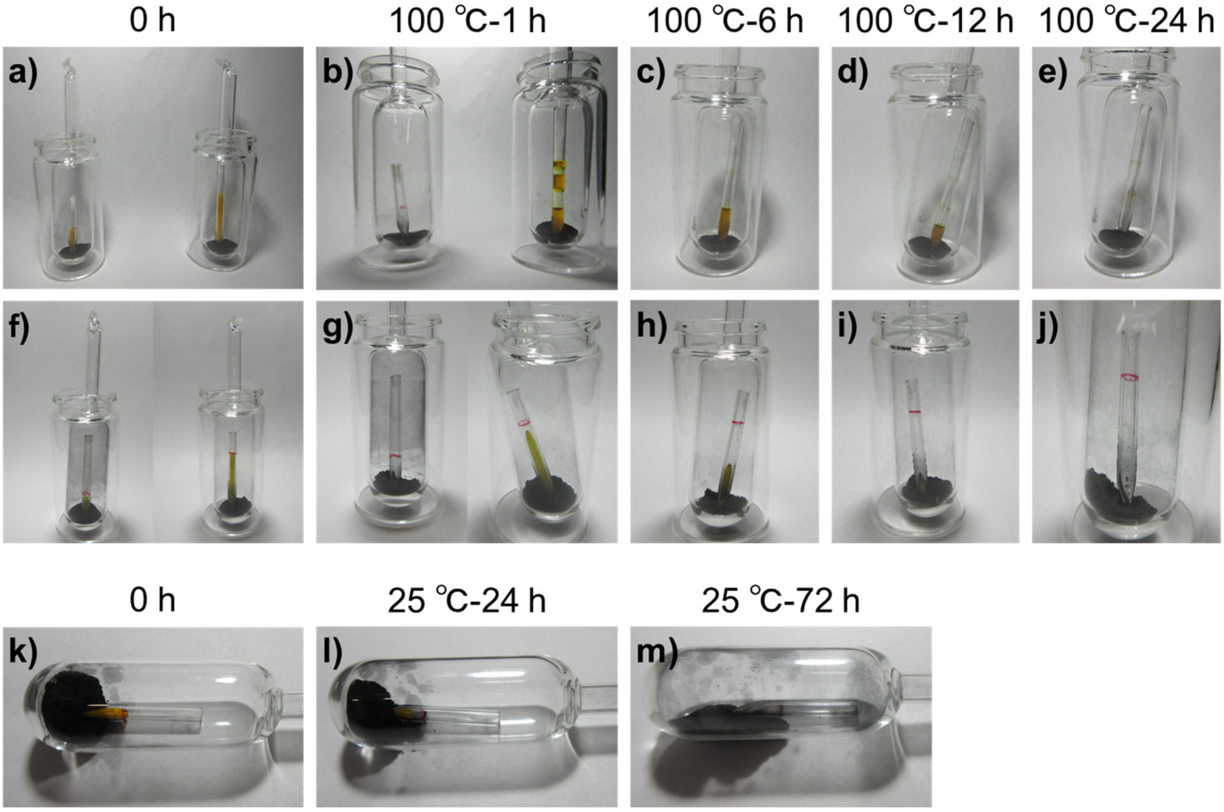

Fig. S4 (a–j) Photographs of sealed glass ampoules containing (a–e) AC and DBBQ and (f–j) AC and TMBQ before and after heating at 100 °C. (a, f) before heating; (b, g) after 1 h; (c, h) after 6 h; (d, i) after 12 h; (e, j) after 24 h. (a, b, f, g) contain 1 mmol (left) and 3 mmol (right) of QD per gram of AC; (c–e, h–j) 3 mmol of QD per gram of AC. (k–m) Photographs of sealed glass ampoules containing AC and DBBQ before and after standing at 25 °C: (k) before standing; (l) after 1 day; (m) after 3 days. Because the melting point of DBBQ is 66.0 °C, it existed in a liquid state inside the capillary at 100 °C (b–d).

As shown in Fig. S3a–j, in the indirect method, the adsorption of 1 and 3 mmol of DBBQ or TMBQ per gram of AC at 100 °C was completed within approximately 1 h and more than 12 h, respectively. In contrast, at 25 °C, the adsorption of 1 mmol of DBBQ per gram of AC required about 3 days to reach completion, whereas the direct method enabled complete adsorption within a very short time even at 25 °C (Fig. 2), demonstrating its remarkable efficiency compared with the indirect method (Scheme 1a).

S5. Temperature-programmed desorption (TPD) analysis

A temperature-programmed desorption (TPD) measurement of AC was carried out using a reactor equipped with a graphite sample holder (pyrolytic carbon-coated graphite, PYROGRAPH, Toyo Tanso, purity 99.9999%) and a quadrupole mass spectrometer (QMS, MPH-100 M, Inficon Co., Ltd.) connected to a calibrated gas reservoir for quantitative detection of CO and CO_2. Prior to use, the reactor and sample holder were cleaned by heating at 1600 °C for 1 h under vacuum ($<3 \times 10^{-4}$ Pa). Subsequently, 1 mg of AC was placed on the sample holder, and the reactor was evacuated with a turbomolecular pump for 2 h until the pressure reached 2×10^{-5}–4×10^{-4} Pa. A TPD measurement was then conducted by heating the sample from room temperature to 1600 °C at 10 °C min^{-1} under vacuum, while monitoring the evolution of CO, CO_2, and H_2O with the QMS (Fig. S5). A blank run confirmed that background CO, CO_2, and H_2O signals from the reactor were negligible compared to those from AC. Quantitative analysis of CO, CO_2, and H_2O revealed that the oxygen content of AC was 2.2 wt%.

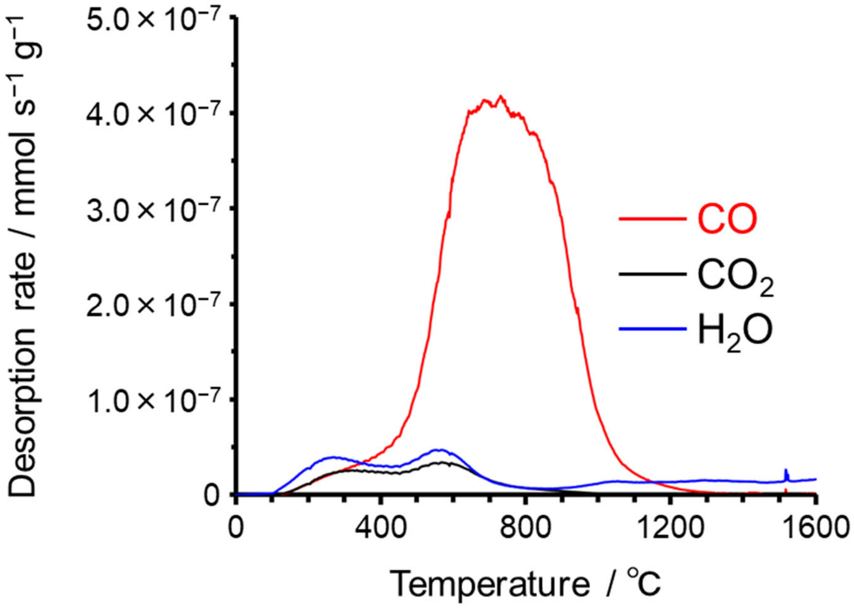

Fig. S5 TPD spectra of AC for CO, CO_2, and H_2O.

S6. N_2 adsorption–desorption measurements of AC/DBBQ hybrids

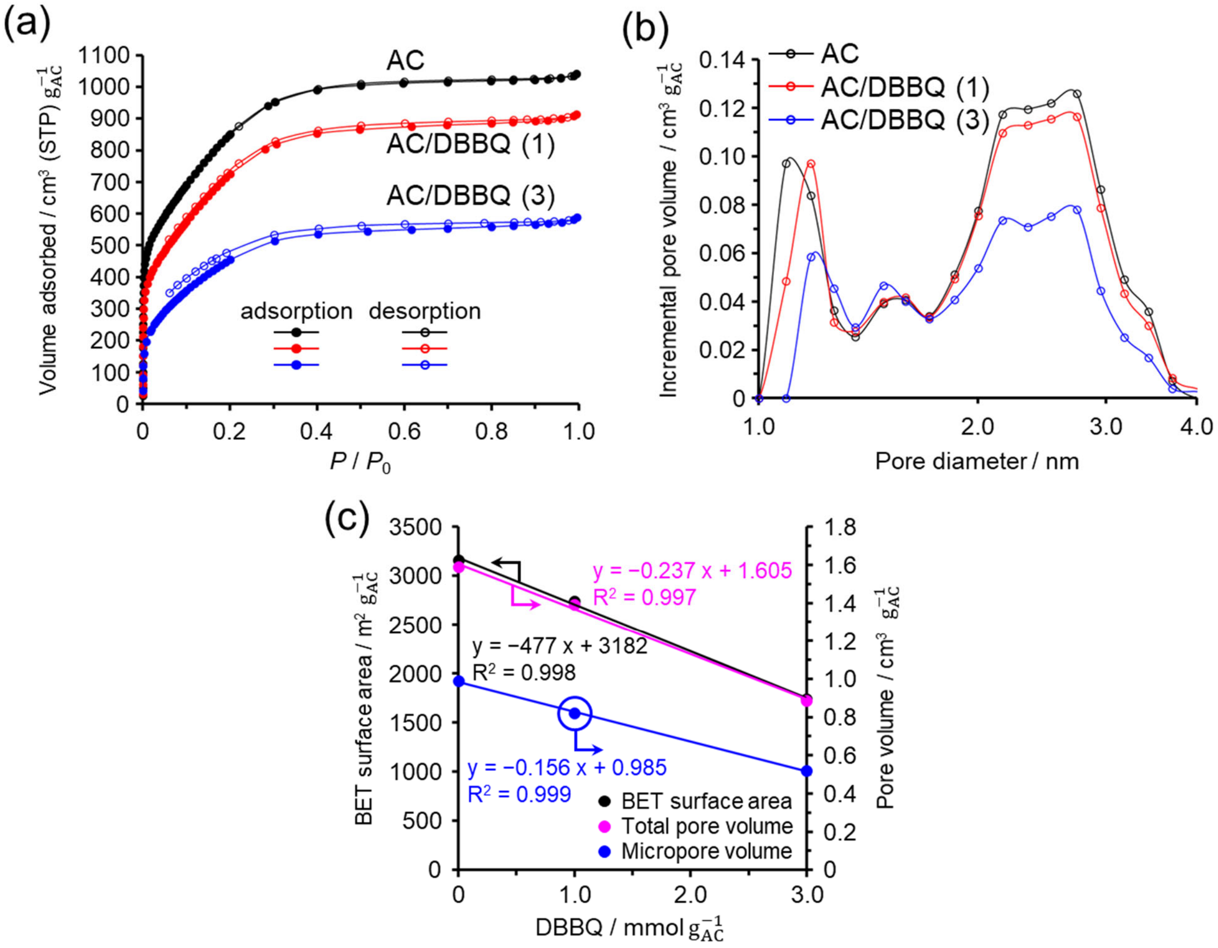

Fig. S6 N_2 adsorption–desorption measurements of AC/DBBQ hybrids, with values normalized per gram of AC. (a) Isotherms, (b) pore size distributions calculated by the density functional theory method for carbon slit pores, and (c) BET specific surface areas and pore volumes as a function of DBBQ content. The values are expressed per gram of AC.

S7. N_2 adsorption–desorption measurements of AC/PBQ hybrids

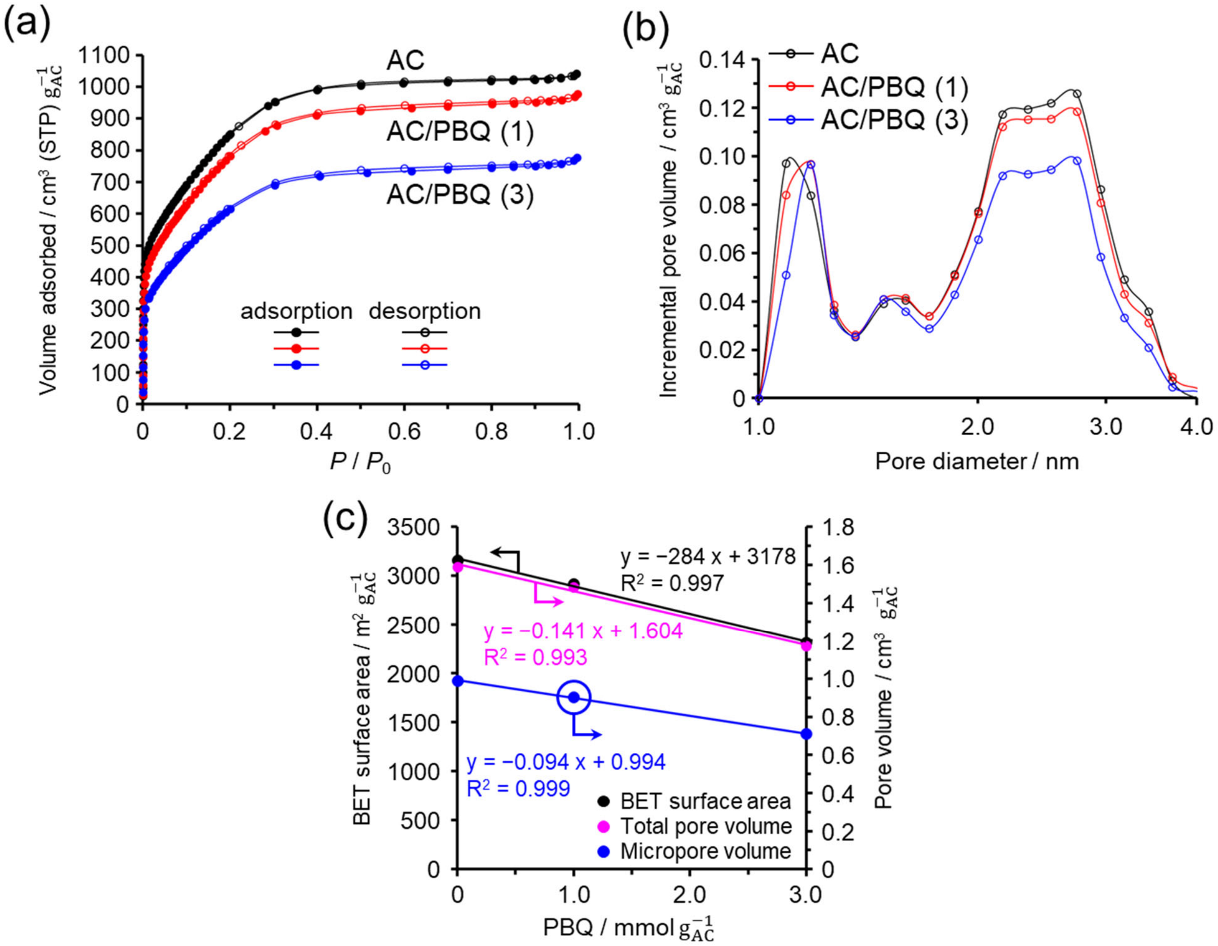

Fig. S7 N_2 adsorption–desorption measurements of AC/PBQ hybrids, with values normalized per gram of AC. (a) Isotherms, (b) pore size distributions calculated by the density functional theory method for carbon slit pores, and (c) BET specific surface areas and pore volumes as a function of PBQ content. The values are expressed per gram of AC.

S8. N_2 adsorption–desorption measurements of AC/NQ hybrids

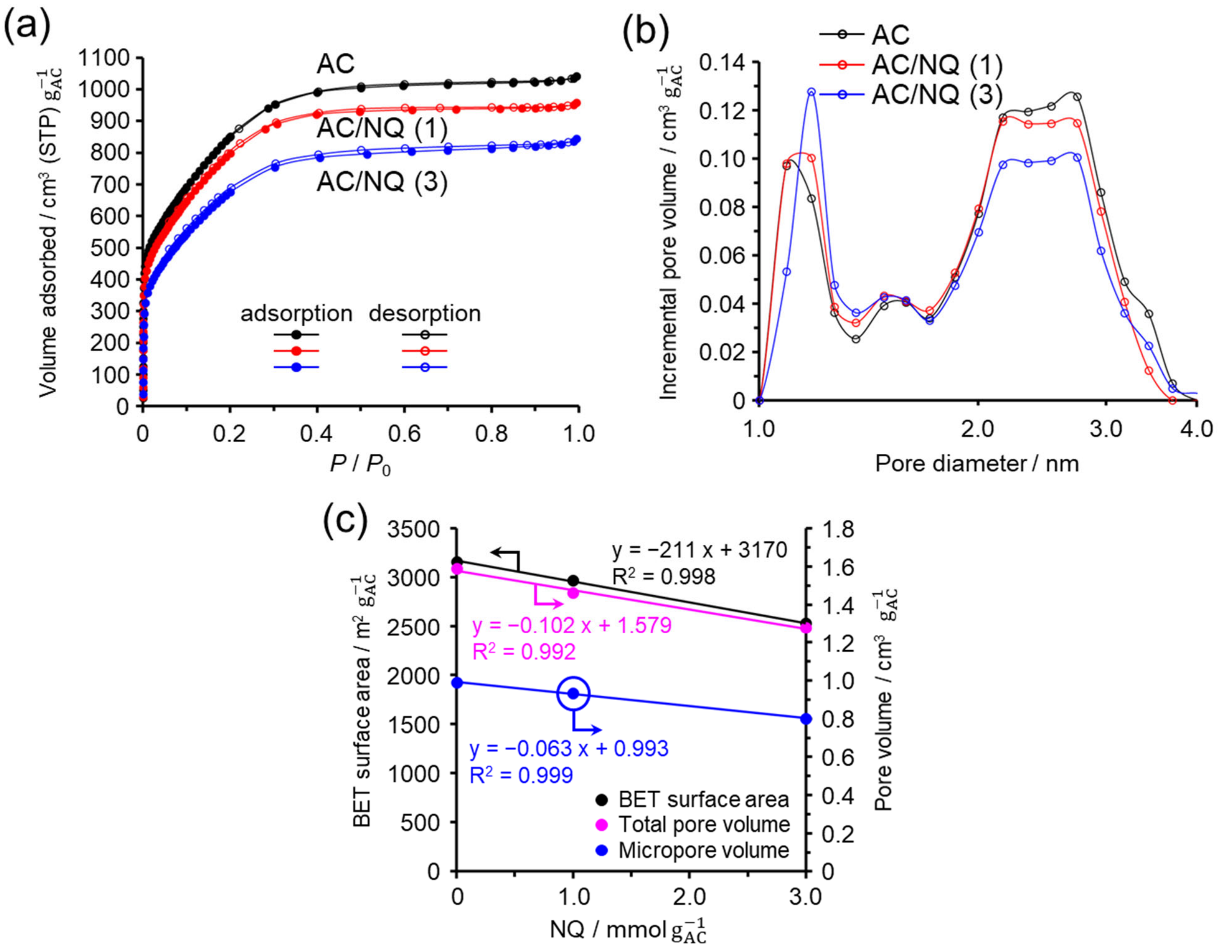

Fig. S8 N_2 adsorption–desorption measurements of AC/NQ hybrids, with values normalized per gram of AC. (a) Isotherms, (b) pore size distributions calculated by the density functional theory method for carbon slit pores, and (c) BET specific surface areas and pore volumes as a function of NQ content. The values are expressed per gram of AC.

S9. Cyclic voltammograms of QDs in 1 M H_2SO_4

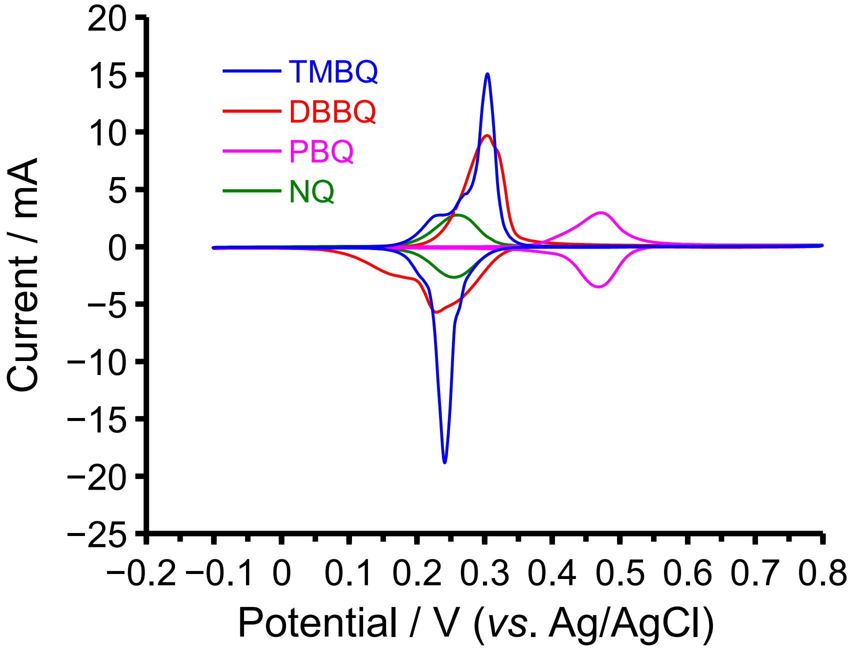

Fig. S9 Cyclic voltammograms of control electrodes prepared by physically mixing each QD (TMBQ, DBBQ, PBQ, and NQ) with conductive carbon black and PTFE binder, measured at 25 °C in 1 M H_2SO_4 using a three-electrode configuration. The scan rate was 1 mV s^{-1} and the potential window was −0.1 to 0.8 V.

S10. Assessment of electrochemically accessible surface area and its stability during cycling

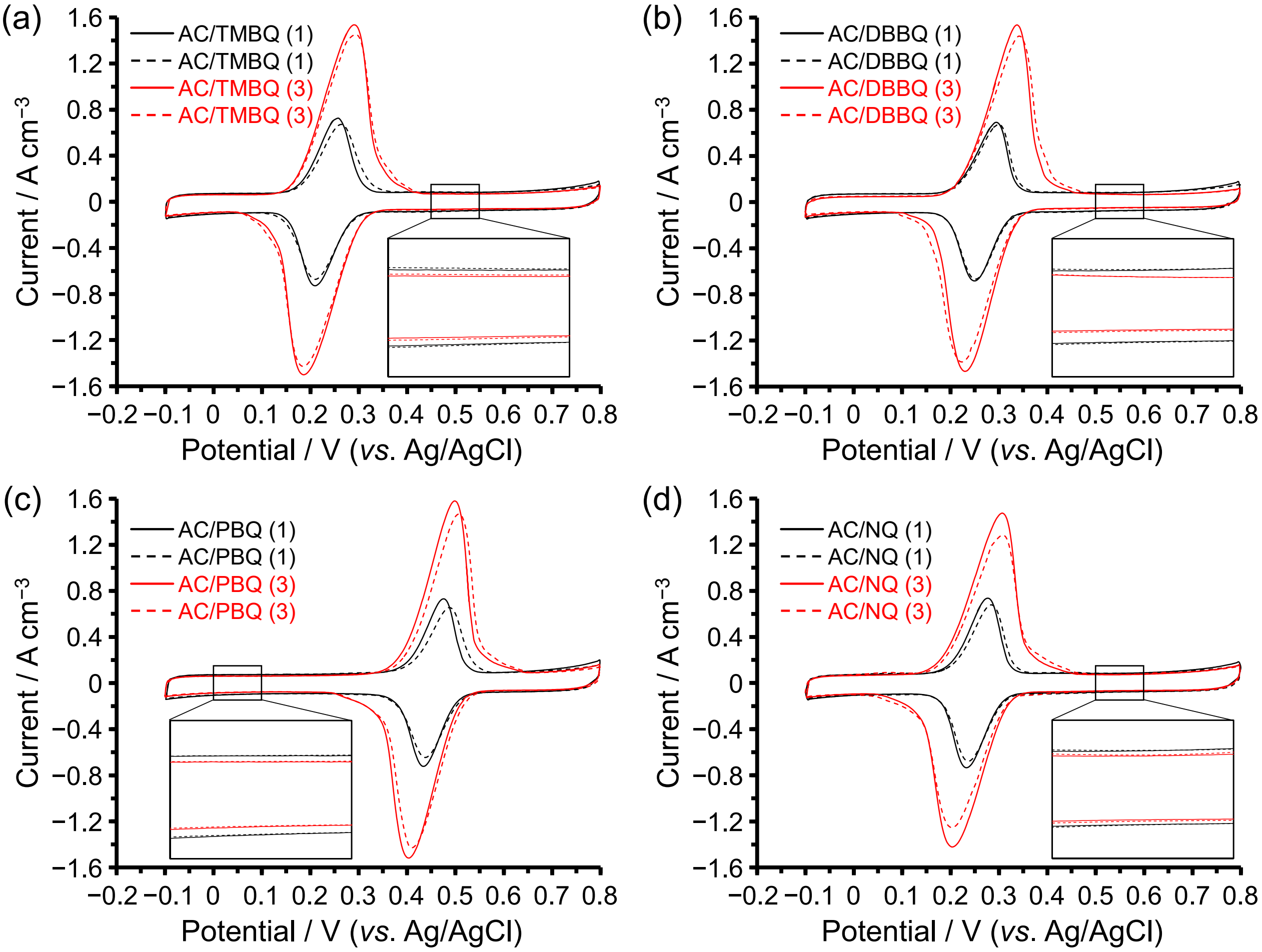

Fig. S10 Cyclic voltammograms of the AC/QD hybrids. The measurements were performed in a three-electrode cell at 1 mV s^{-1} within a potential window of −0.1–0.8 V. The solid lines represent the initial CV recorded before the electrochemical tests, whereas the dashed lines represent the CV recorded after the galvanostatic charge–discharge (GCD) measurements. The CV, EIS, and GCD results obtained during this sequence are shown in Fig. 5 in the main text. Insets show enlarged regions of the voltammograms highlighting the EDL-derived current to facilitate comparison of the electrochemically accessible surface. (a) AC/TMBQ (1) and AC/TMBQ (3); (b) AC/DBBQ (1) and AC/DBBQ (3); (c) AC/PBQ (1) and AC/PBQ (3); (d) AC/NQ (1) and AC/NQ (3). The nearly identical EDL-derived currents before and after GCD measurements indicate that the electrochemically accessible surface area is largely preserved.

S11. Calculation of QD utilization efficiency

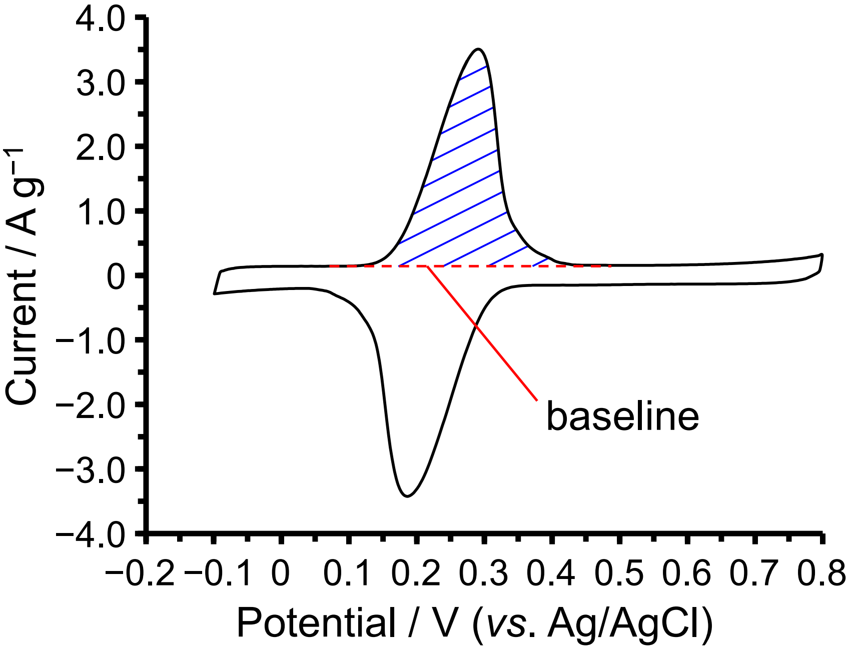

Fig. S11 Calculation of the utilization efficiency of QDs in the AC/QD hybrids using cyclic voltammograms recorded at 1 mV s^{-1}.

The utilization efficiency was calculated from the anodic charge obtained by integrating the redox peak in the cyclic voltammogram recorded at 1 mV s^{-1}. The EDL-derived current was subtracted prior to integration. The theoretical charge was calculated from the amount of hybridized QDs assuming a two-electron redox process. The utilization efficiency was defined as the ratio of experimental charge to theoretical charge.

S12. Dependence of cyclic voltammograms of AC/QD hybrids on sweep rate

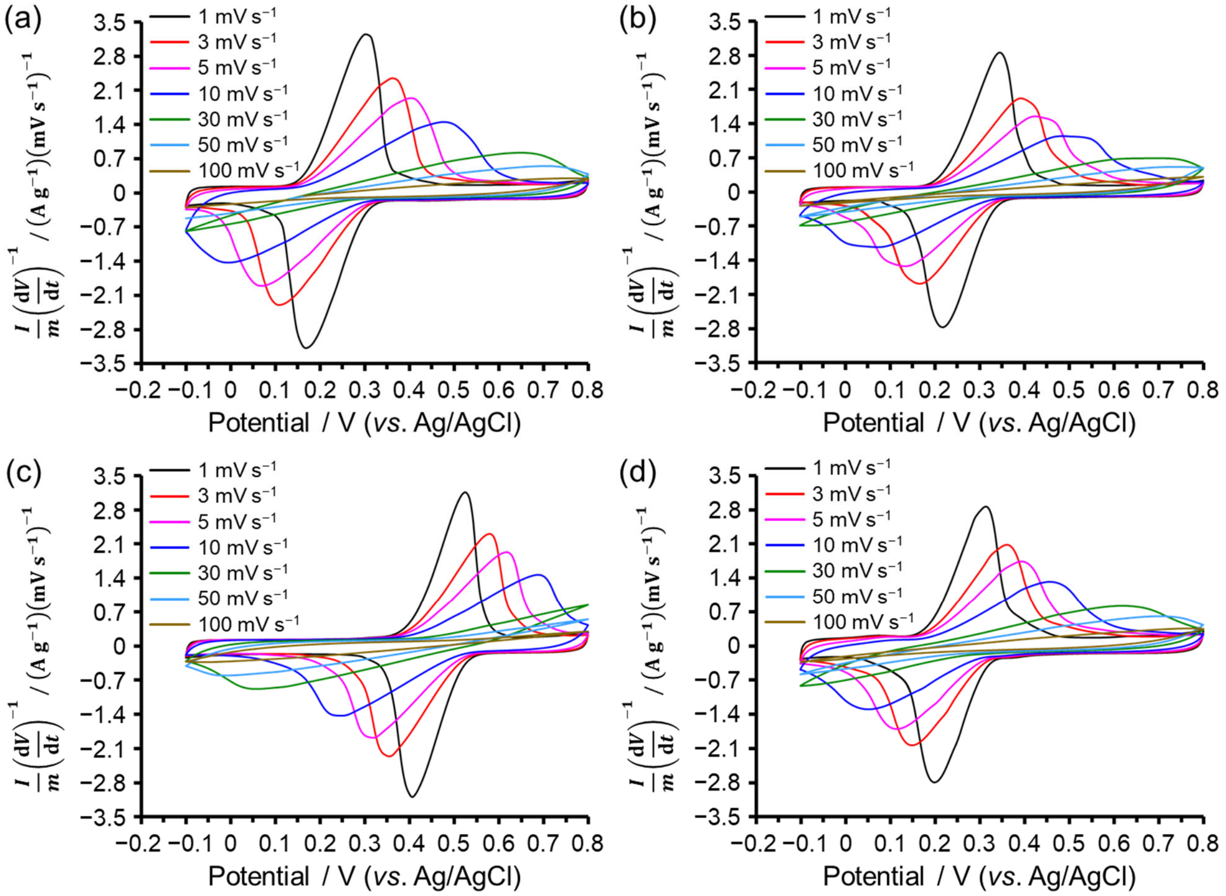

Fig. S12 Cyclic voltammograms of (a) AC/TMBQ (3), (b) AC/DBBQ (3), (c) AC/PBQ (3), and (d) AC/NQ (3) at sweep rates of 1–100 mV s^{-1}.

S13. Trasatti analysis based on scan-rate-dependent cyclic voltammetry

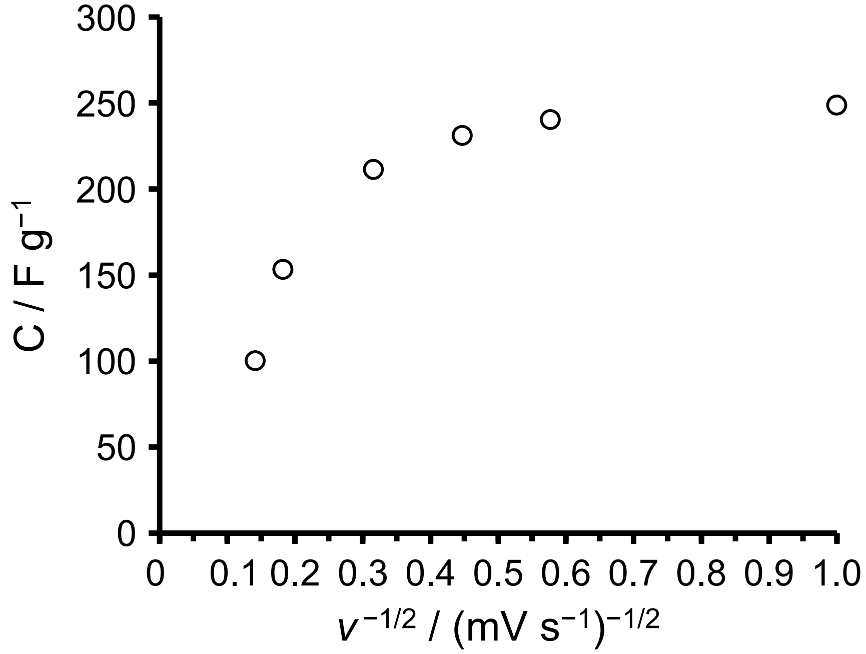

Fig. S13 Trasatti plot for AC/TMBQ (3) based on scan-rate-dependent CVs (1–50 mV s^{-1}), shown as *C* vs $v^{-1/2}$, where *C* is the gravimetric capacitance (F g^{-1}) obtained from CV integration and *v* is the scan rate (mV s^{-1}).

Trasatti-type plots were constructed using the gravimetric capacitance derived from CV integration (1–50 mV s^{-1}, Fig. S12a). The plots did not show a clear linear relationship within the measured scan-rate range, indicating that the assumptions required for reliable extrapolation are not fully satisfied for this redox-active AC/QD electrode; hence, the analysis is provided only as a qualitative reference.

S14. Nyquist plots of AC and AC/QD hybrid measured at different applied potentials.

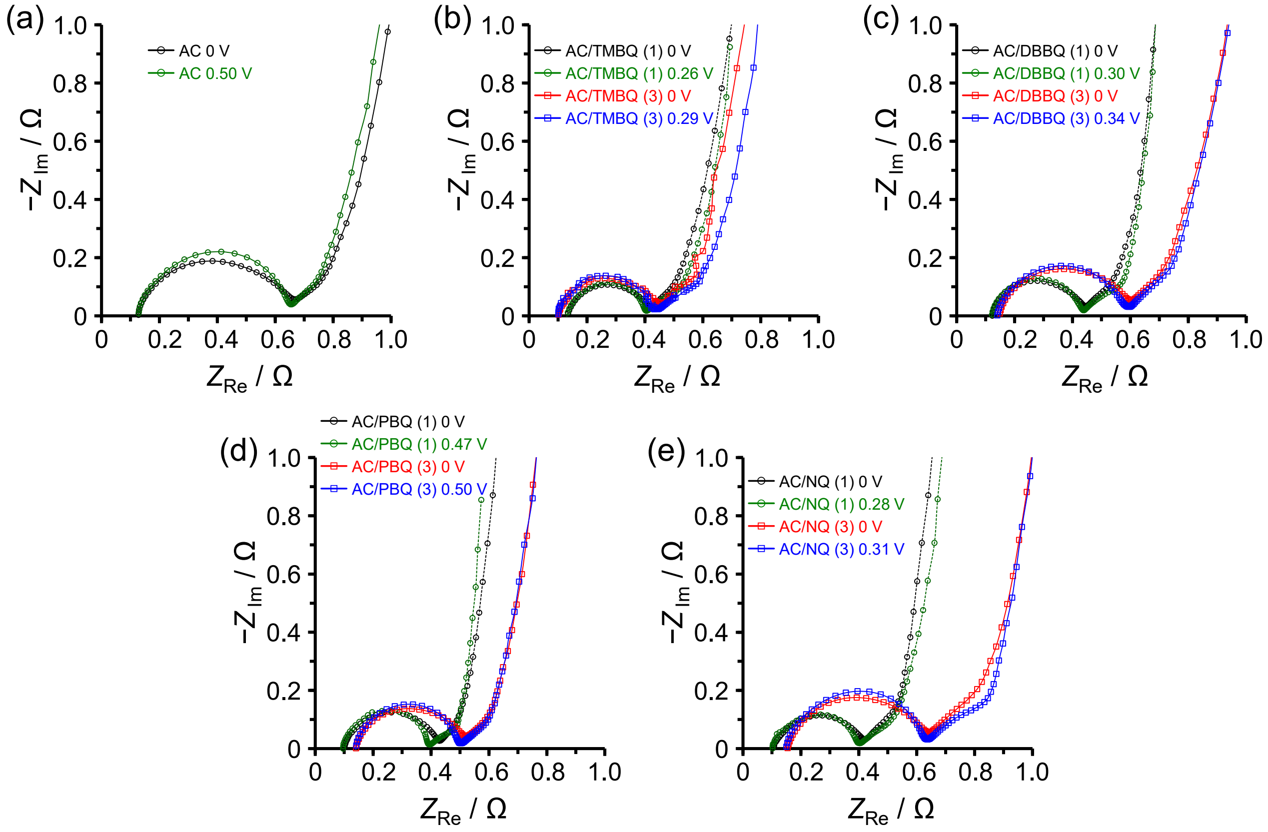

Fig. S14 Nyquist plots of (a) AC, (b) AC/TMBQ hybrids, (c) AC/DBBQ hybrids, (d) AC/PBQ hybrids, and (e) AC/NQ hybrids measured at two different applied potentials (at the QD anodic peak potential and at a potential outside the redox region, 0 V *vs*. Ag/AgCl). The measurements were performed in a three-electrode cell at 25 °C.

S15. Galvanostatic charge–discharge curves of AC, AC/TMBQ (3), and AC/DBBQ (3)

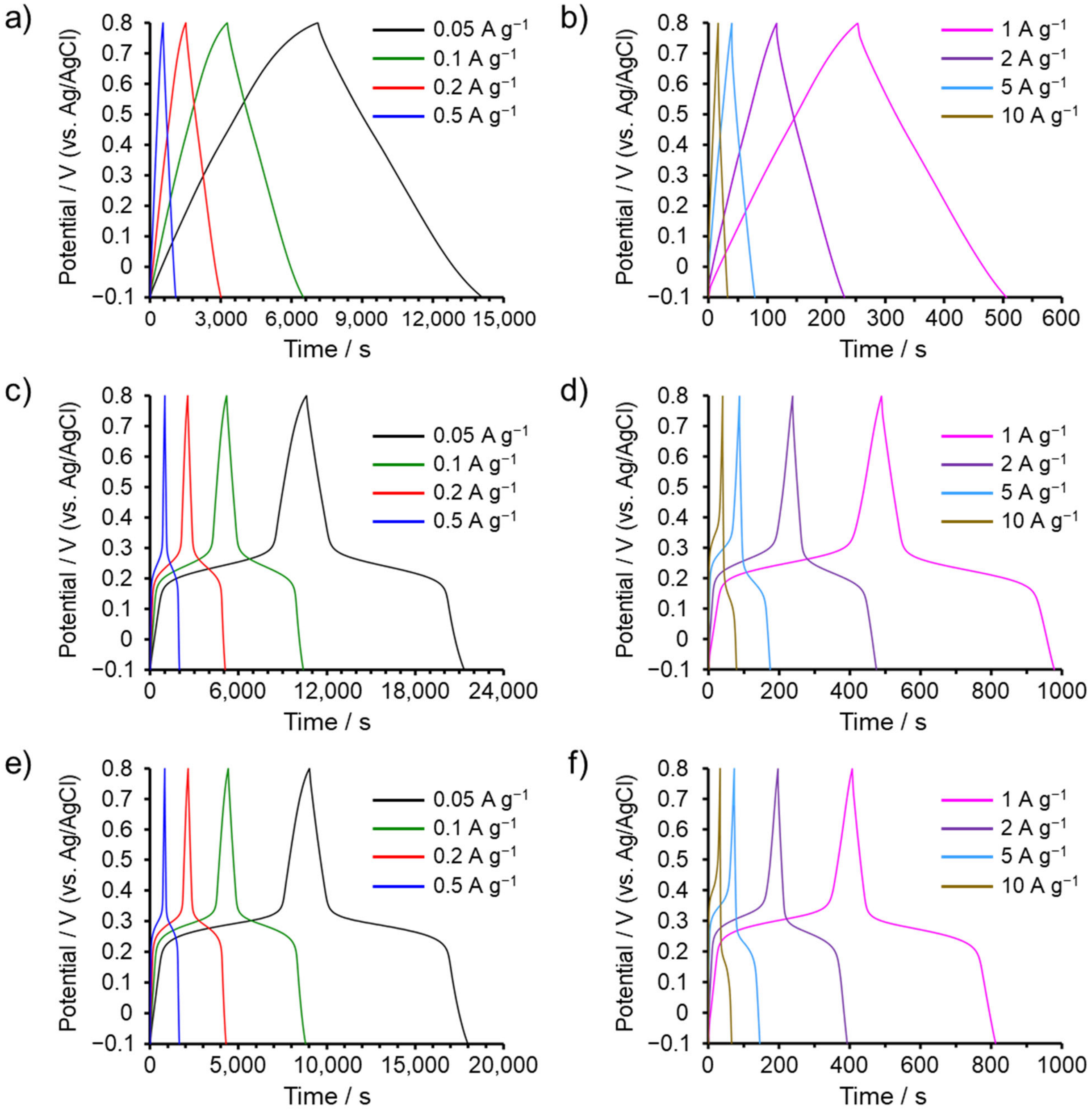

Fig. S15 Galvanostatic charge–discharge (GCD) curves of (a, b) AC, (c, d) AC/TMBQ (3), and (e, f) AC/DBBQ (3). The measurements were performed in a three-electrode cell at 25 °C.

S16. Galvanostatic charge–discharge curves of AC/PBQ (3) and AC/NQ (3)

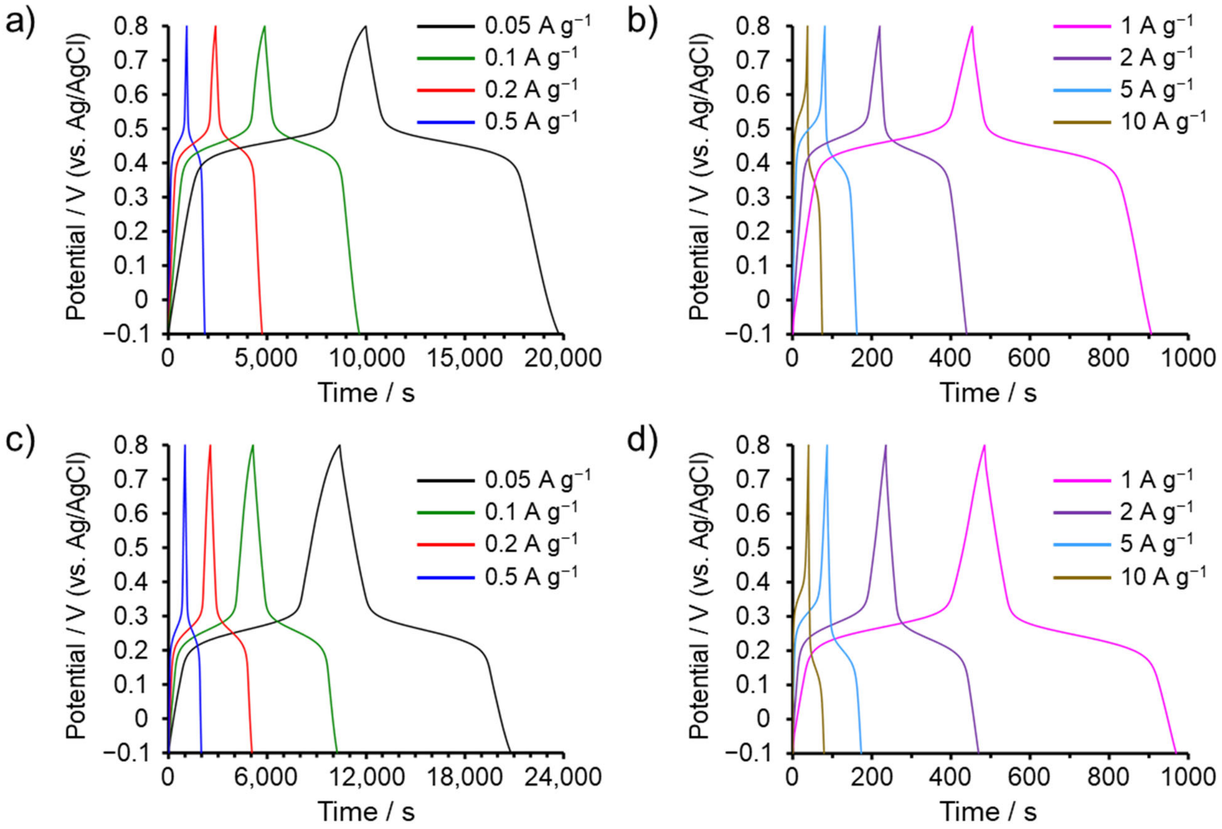

Fig. S16 GCD curves of (a, b) AC/PBQ (3) and (c, d) AC/NQ (3). The measurements were performed in a three-electrode cell at 25 °C.

Table S1 Comparison of capacitances obtained from GCD (0.5 A g^{-1}) and CV (1 mV s^{-1}) within the potential window of −0.1 to 0.8 V measured in a three-electrode cell.

Samples	GCD results (0.5 A g^{-1})		CV results (1 mV s^{-1})
	C_v [F cm^{-3}]	Time [s] [a]	C_v [F cm^{-3}] [b]
AC	89.4	545	91.0
AC/TMBQ (1)	142.3	749	137.5
AC/TMBQ (3)	242.2	995	243.0
AC/DBBQ (1)	133.5	670	132.5
AC/DBBQ (3)	224.2	833	220.6
AC/PBQ (1)	139.6	723	140.7
AC/PBQ (3)	234.0	925	235.5
AC/NQ (1)	139.2	736	142.7
AC/NQ (3)	238.0	985	247.0

[a] Time required for the potential change from −0.1 to 0.8 V in the GCD measurement.

[b] Time required for the potential sweep from −0.1 to 0.8 V at 1 mV s^{-1} was 900 s for all samples.

S17. Reproducibility of the electrochemical performance of independently prepared AC/QD Hybrids

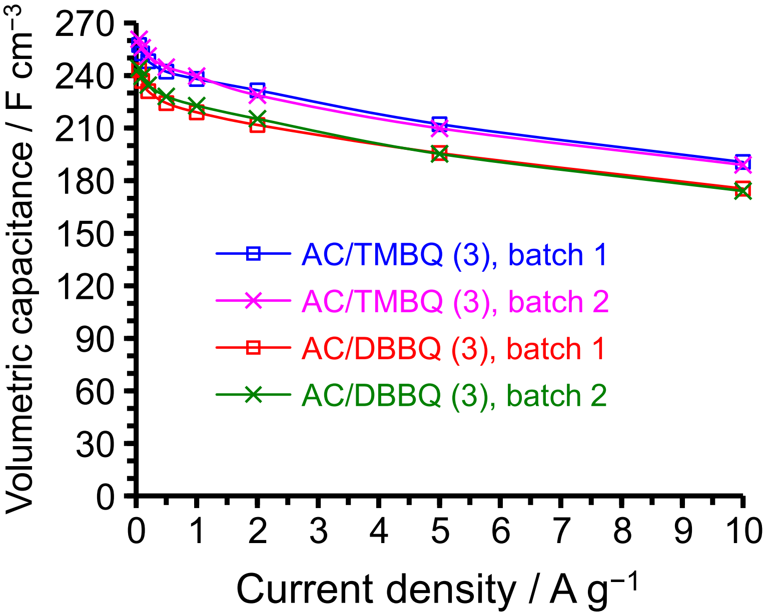

Fig. S17 Volumetric capacitance (F cm^{-3}) as a function of current density for AC/TMBQ (3) and AC/DBBQ (3) hybrids prepared from two independent batches (batch 1 and batch 2), demonstrating the reproducibility of the hybrid preparation. The measurements were performed in a three-electrode cell at 25 °C.

S18. Electrochemical behavior of AC/TMBQ (3) and AC/DBBQ (3) prepared by the indirect method at 100 °C

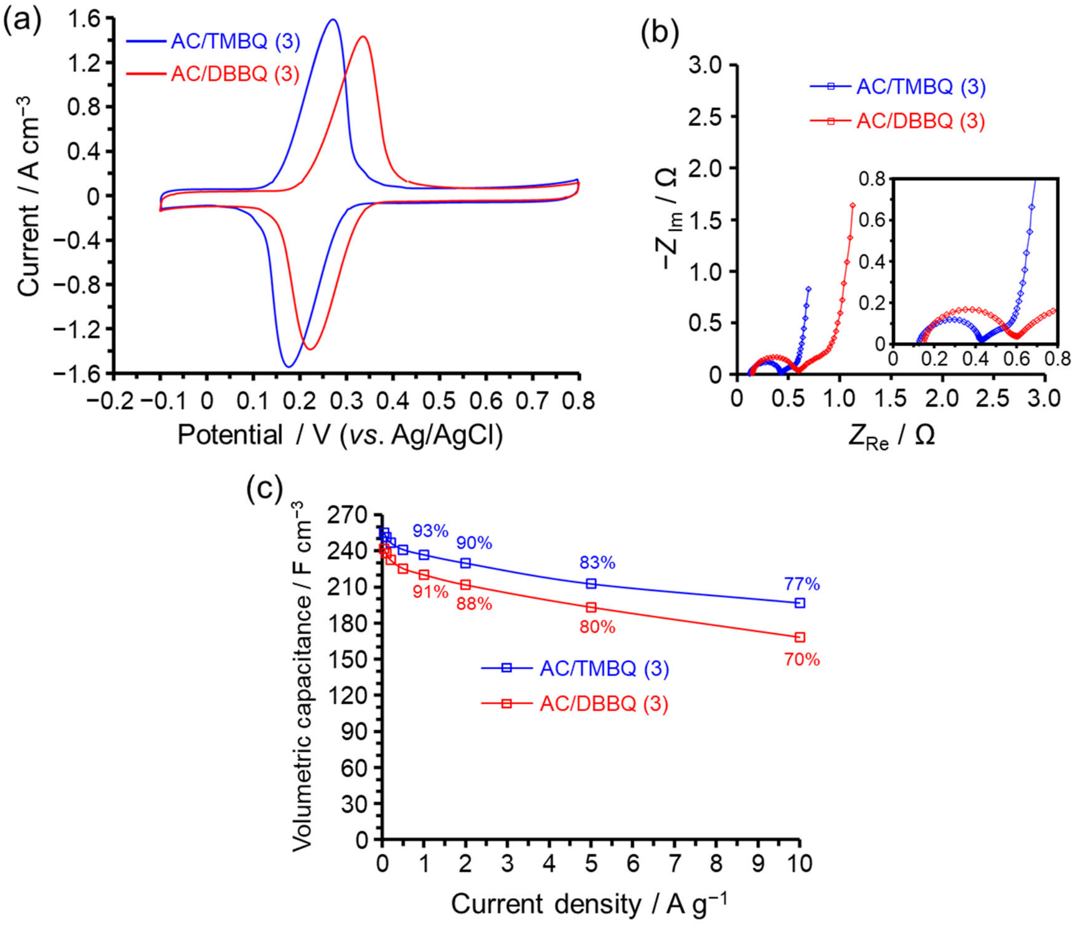

Fig. S18 (a) Cyclic voltammograms at 1 mV s^{-1} in the potential range of −0.1 to 0.8 V, (b) Nyquist plots, and (c) volumetric capacitances as a function of current density, derived from GCD measurements in the potential range of −0.1 to 0.8 V. All measurements were performed in a three-electrode cell at 25 °C.

As shown in Fig. S11, the AC/DBBQ (3) prepared by the indirect method exhibited slightly lower capacitance retention than the other AC/QD hybrids (Fig. S11c). This behavior is consistent with the hindered ion diffusion caused by the two bulky *tert*-butyl groups in DBBQ, which also leads to a concomitant retardation of charge transfer (Fig. S11b). The electrochemical behaviors of AC/TMBQ (3) and AC/DBBQ (3) prepared by the indirect method were consistent with those of the corresponding samples prepared by the direct method (Fig. 5).

S19. Electrochemical behavior of AC/TMBQ (3) and AC/PBQ (3) prepared by the direct method at 25 °C without drying of AC

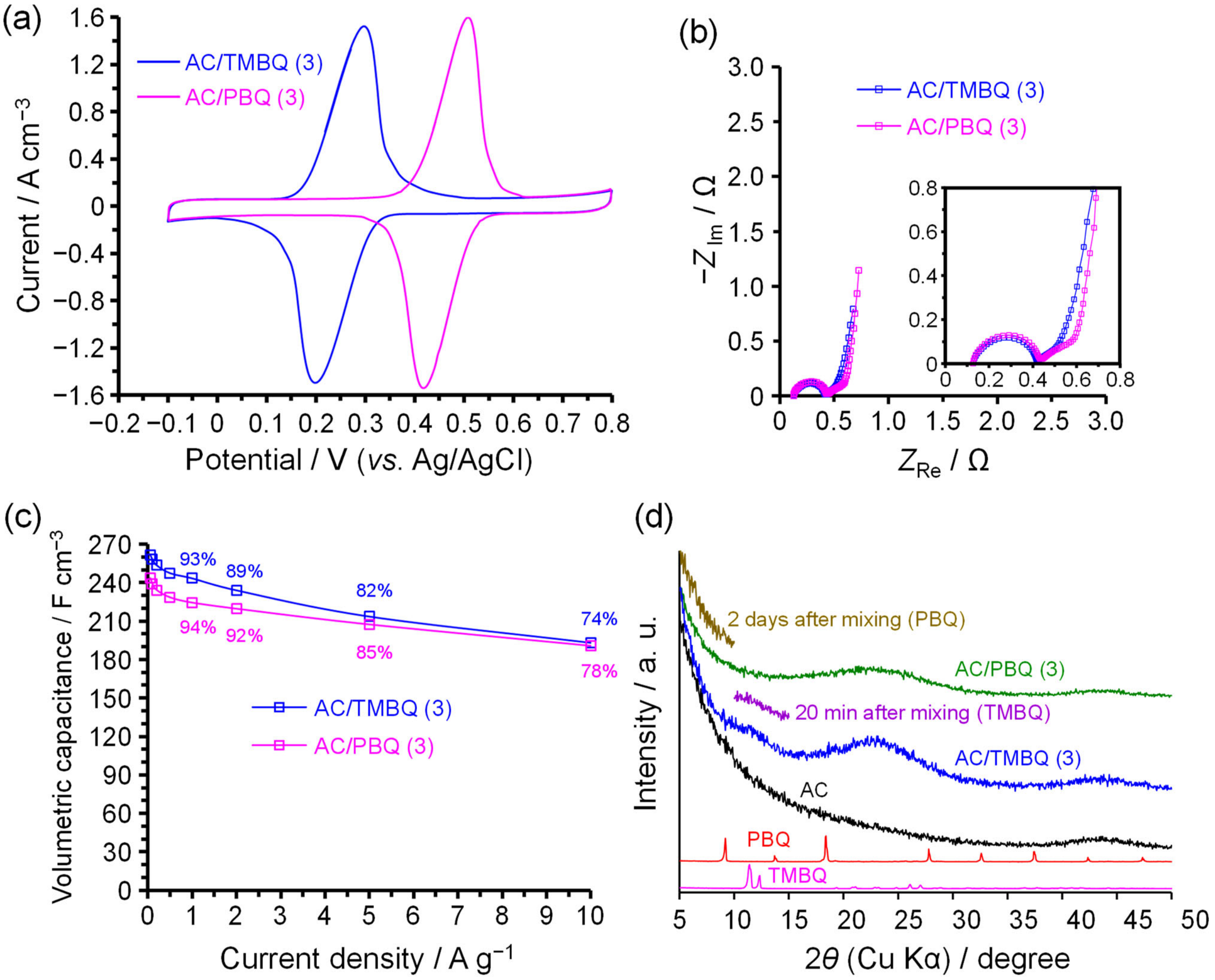

Fig. S19 (a) Cyclic voltammograms at 1 mV s^{-1} in the potential range of −0.1 to 0.8 V, (b) Nyquist plots, and (c) volumetric capacitances as a function of current density, derived from GCD measurements in the potential range of −0.1 to 0.8 V. All electrochemical measurements were performed in a three-electrode cell at 25 °C. (d) XRD patterns of AC, the QDs, their mixtures at different adsorption times, and the AC/QD hybrids (after complete adsorption). The QDs used were TMBQ and PBQ.

S20. Initial electrochemical behavior of AC/TMBQ (3) and AC/PBQ (3) electrodes

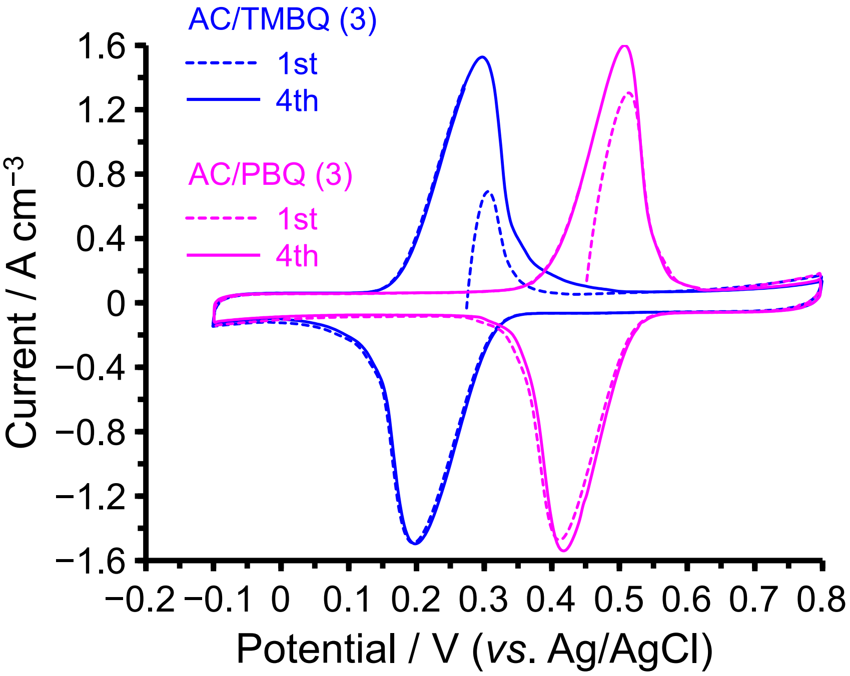

Fig. S20 Cyclic voltammograms of AC/TMBQ (3) and AC/PBQ (3) measured in a three-electrode cell under the same conditions as those used for Fig. 5a. The first cycle (dashed line) and the fourth cycle (solid line) are shown to illustrate the evolution of the electrochemical response during the initial cycles.

S21. GCD profiles of AC||AC and AC/TMBQ (3)||AC/PBQ (3) coin cells

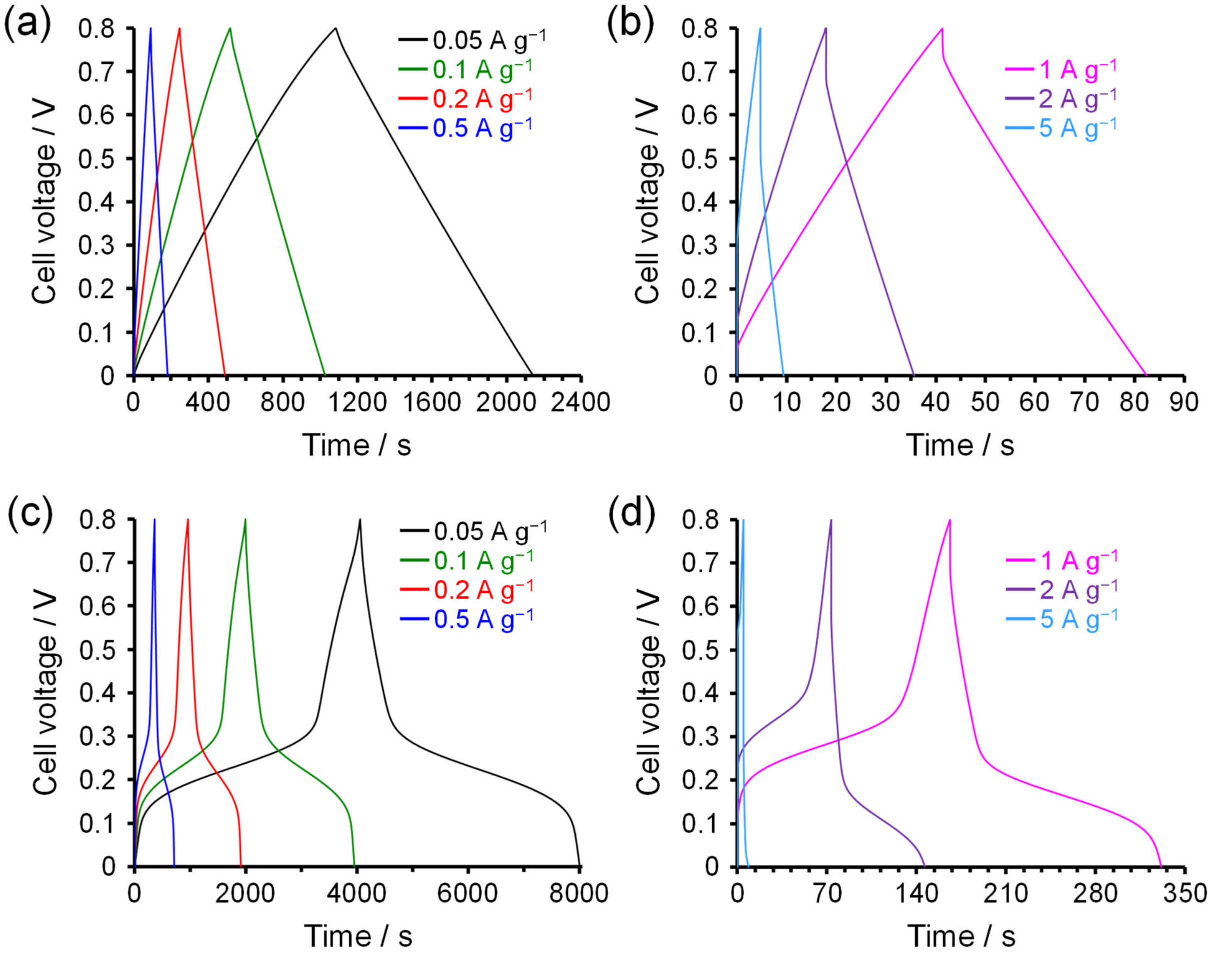

Fig. S21 Galvanostatic charge–discharge (GCD) curves of (a, b) the symmetric AC||AC cell and (c, d) the AC/TMBQ (3)||AC/PBQ (3) asymmetric cell measured under the same conditions as those used for Fig. 6.

S22. Structural characterization and electrochemical performance of YP-50F

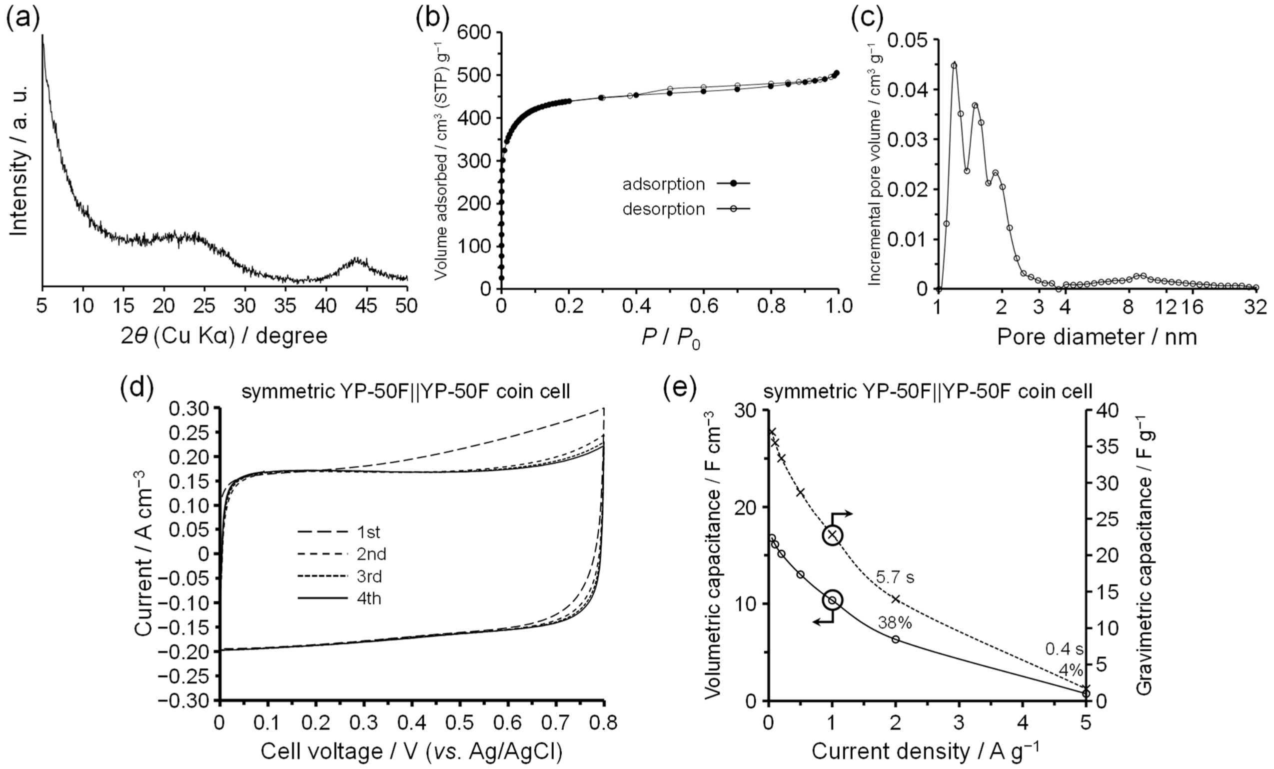

Fig. S22 Structural characterization and electrochemical performance of YP-50F: (a) XRD pattern; (b) N_2 adsorption–desorption isotherm measured at −196 °C; (c) pore size distribution derived from the N_2 adsorption data using the DFT method assuming slit-shaped carbon pores; (d) cyclic voltammograms; and (e) gravimetric and volumetric capacitances as a function of current density. Electrochemical measurements were conducted under the same conditions as those in Fig. 5a.

S23. Current dependence of the IR drop (ΔV_{IR}) and mean cell voltage (V_{mean}) for symmetric AC||AC, asymmetric AC/TMBQ (3)||AC/PBQ (3), and symmetric YP-50F||YP-50F coin cells.

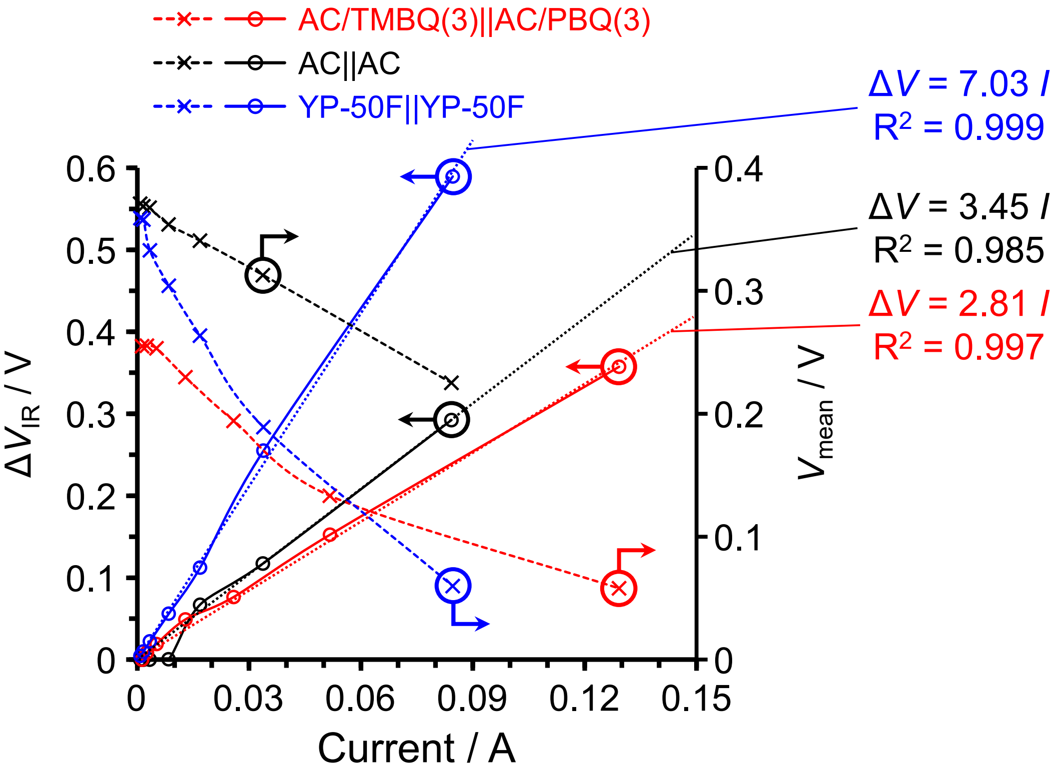

Fig. S23 Current dependence of the IR drop (ΔV_{IR}) and the mean cell voltage (V_{mean}) obtained from galvanostatic charge–discharge measurements for the symmetric AC||AC, asymmetric AC/TMBQ (3)||AC/PBQ (3), and symmetric YP-50F||YP-50F coin cells. The left axis represents ΔV_{IR}, and the right axis represents V_{mean}. The dashed lines represent linear fits of ΔV_{IR} as a function of current ($\Delta V_{\mathrm{IR}} = IR$), yielding internal resistances of 3.45 Ω ($R^2 = 0.985$) for the symmetric AC||AC coin cell, 2.81 Ω ($R^2 = 0.997$) for the asymmetric AC/TMBQ (3)||AC/PBQ (3) cell, and 7.03 Ω ($R^2 = 0.999$) for the symmetric YP-50F||YP-50F cell. The V_{mean} was calculated as the time-averaged voltage during discharge from immediately after the IR drop to 0 V.

S24. Current-density dependence of areal, volumetric, and gravimetric capacitance and capacity derived from GCD measurements of AC and AC/QD hybrid electrodes.

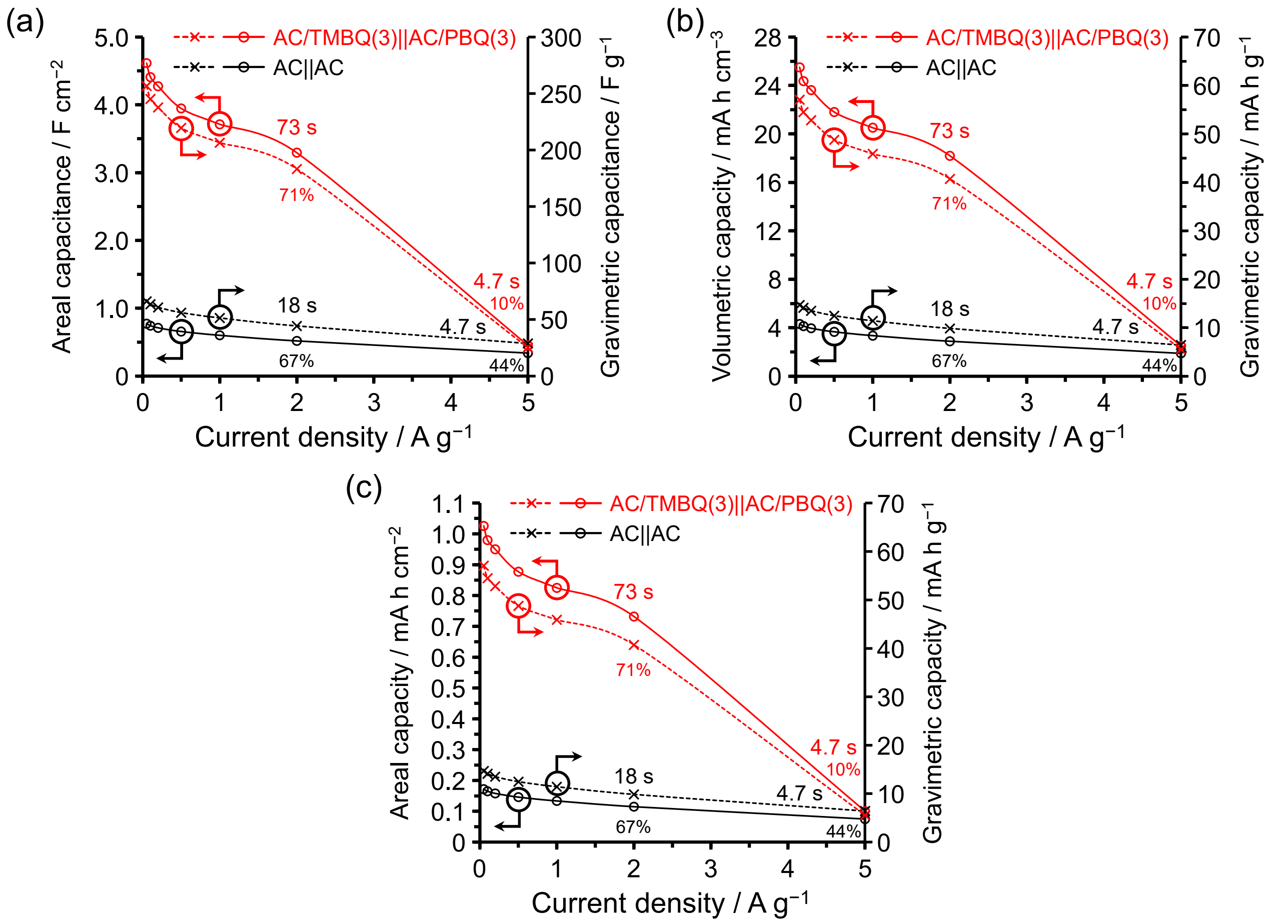

Fig. S24 Current-density dependence of electrochemical performance metrics derived from GCD measurements: (a) areal capacitance (F cm^{-2}) and gravimetric capacitance (F g^{-1}), (b) volumetric capacity (mAh cm^{-3}) and gravimetric capacity (mAh g^{-1}), and (c) areal capacity (mAh cm^{-2}) and gravimetric capacity (mAh g^{-1}) for AC and AC/QD hybrid electrodes. The capacity values were calculated from the corresponding capacitances using $Q = C\,\Delta V$ (1 mAh = 3.6 C) with a voltage window of $\Delta V = 0.8$ V.

S25. Cycling and aging behavior of AC/TMBQ(3)||AC/PBQ(3) coin cells

To clarify the influence of electrochemical pretreatment and calendar ageing on the cycling behavior of the AC/TMBQ (3)||AC/PBQ (3) coin cell, additional cycle tests were conducted under the following conditions: (i) immediate cycling after cell assembly without pretreatment, (ii) after four CV cycles at 1 mV s^{-1} between 0 and 0.8 V, (iii) after four GCD cycles at 0.1 A g^{-1} between 0 and 0.8 V, (iv) after storage at 25 °C for 17 days, (v) after storage at 25 °C for 17 days followed by four CV cycles, (vi) after storage at 25 °C for 17 days followed by four GCD cycles, (vii) after storage at 25 °C for one month. These results are compared with that obtained after four CV cycles and four GCD cycles, corresponding to the protocol used for Fig. 6. The results obtained under these conditions are shown in Fig. S25a.

The results show that the first-cycle capacitance strongly depends on the pretreatment history of the coin cell. When cycling was initiated immediately after cell assembly, the first-cycle volumetric capacitance was only 0.6 F cm^{-3}, whereas the capacitance increased markedly during subsequent cycles. In contrast, the cell subjected to four CV and four GCD cycles before the cycling test exhibited the best overall cycling performance, with 91.9 F cm^{-3} in the first cycle and 73.9 F cm^{-3} after 10,000 cycles. Cells subjected only to four CV cycles or four GCD cycles before cycling also showed much higher first-cycle capacitances than the immediately cycled cell. Similar tendencies were observed after storage for 17 days at 25 °C, indicating that both electrochemical pretreatment and storage history affect the initial electrochemical state of the coin cell.

Importantly, the same tendency was also observed for symmetric AC||AC coin cells (Fig. S25b). When the AC||AC cell was cycled immediately after assembly, the volumetric capacitance was 8.9 F cm^{-3} in the first cycle and 12.1 F cm^{-3} after 10,000 cycles, whereas under the Fig. 6 protocol (after four CV and four GCD cycles), the corresponding values were 15.4 and 15.7 F cm^{-3}. A similar result was also obtained for the YP-50F||YP-50F coin cell, which showed 8.2 F cm^{-3} in the first cycle and 11.5 F cm^{-3} after 10,000 cycles when cycled immediately after assembly. These results indicate that the low initial capacitance is not unique to the quinone-modified cell, but is mainly related to the electrochemical conditioning process of the coin cell system with a limited amount of electrolyte.

To investigate the possibility of quinone redistribution during storage and cycling, the negative and positive electrodes were removed from the assembled coin cells after storage or after the cycling tests, and each recovered electrode was re-evaluated by CV in a three-electrode configuration (Fig. S26 and S27). The initial utilization efficiencies of TMBQ in AC/TMBQ (3) and PBQ in AC/PBQ (3), calculated from the voltammograms in Fig. 5a, were 94% and 87%, respectively (Table 3). After storage of the

AC/TMBQ (3)||AC/PBQ (3) coin cell at 25 °C for 17 days, small redox peaks assignable to PBQ were observed in the recovered negative electrode, while small redox peaks assignable to TMBQ were observed in the recovered positive electrode (Fig. S27a). These observations indicate that PBQ was partially desorbed from the positive electrode and adsorbed onto the negative electrode, whereas TMBQ was partially desorbed from the negative electrode and adsorbed onto the positive electrode during storage. To quantify this behavior, the peak areas attributed to TMBQ and PBQ were separately integrated for each recovered electrode, as explained in Section S11 (Fig. S11). Because the electrodes deform slightly upon removal, the cyclic voltammograms become somewhat distorted (Fig. S26 and S27), compared with those shown in Fig. 5a. Therefore, when the anodic peaks derived from TMBQ and PBQ overlapped, the integration was performed using the cathodic peaks instead. Here, "N" and "P" denote the negative and positive electrodes, respectively. The resulting utilization efficiencies after storage for 17 days were N) TMBQ 80%, PBQ 11%, and P) TMBQ 14%, PBQ 60%.

The same analysis was performed for the electrodes recovered after the additional cycling tests under conditions (i)–(vii), and the resulting utilization efficiencies are summarized in Table S2. For example, immediately cycled cells showed N) TMBQ 90%, PBQ 9%, and P) TMBQ 5%, PBQ 72%, whereas after storage for one month at 25 °C, the values changed to N) TMBQ 77%, PBQ 13%, and P) TMBQ 17%, PBQ 55%. However, because the major fraction of each quinone still remained in its original electrode even after long-term storage or cycling, the moderate capacitance decrease during 10,000 cycles is most likely associated with the gradual desorption and redistribution of quinone species between the electrodes rather than their irreversible decomposition.

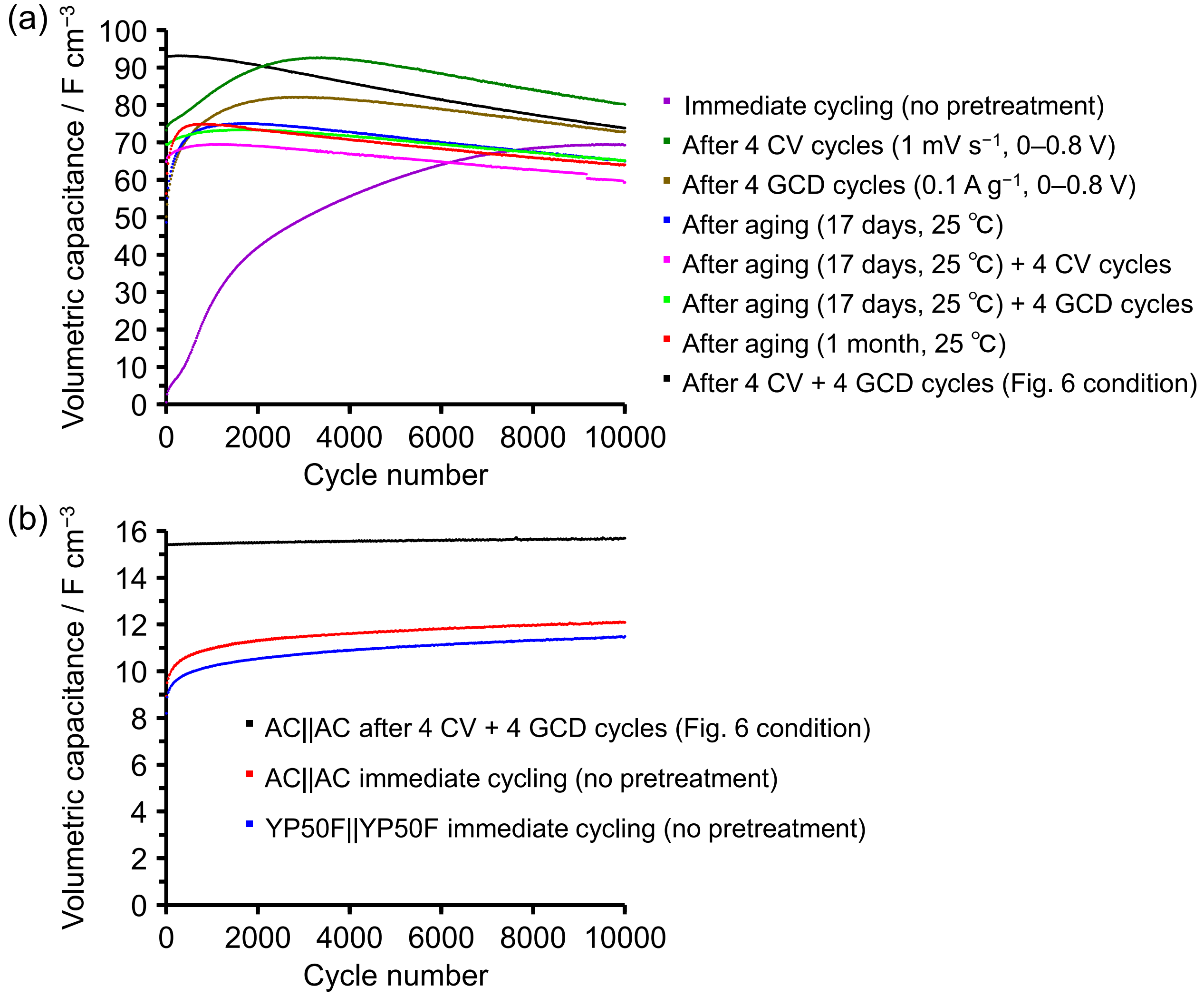

Fig. S25 Cycling performance measured at 2 A g^{-1} within a cell voltage window of 0–0.8 V: (a) AC/TMBQ (3) (negative)||AC/PBQ (3) (positive) coin cell and (b) symmetric AC||AC and YP-50F||YP-50F coin cells.

S26. Cyclic voltammetric behavior of AC/TMBQ (3) and AC/PBQ (3) electrodes after cycling and aging

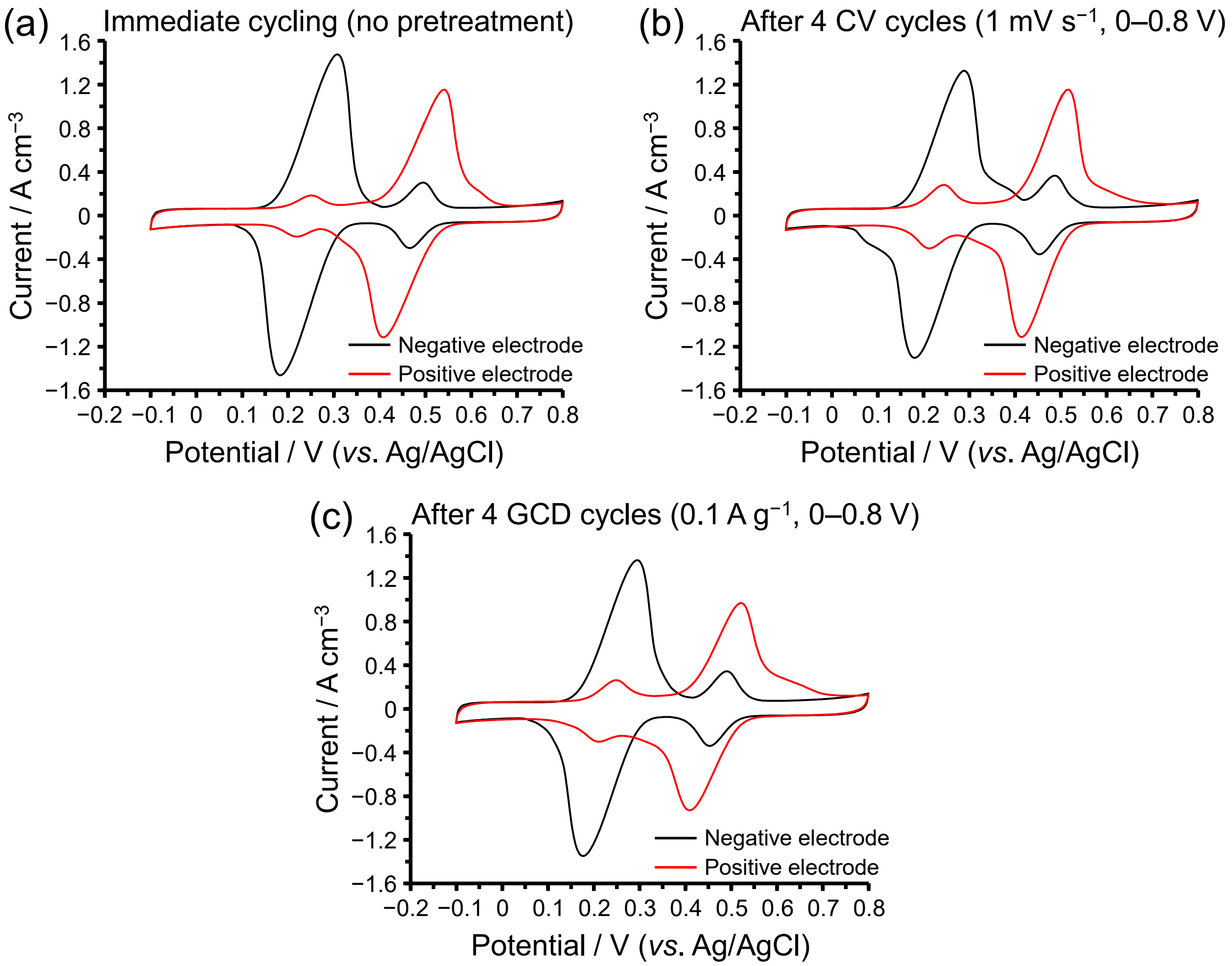

Fig. S26 Cyclic voltammograms of the negative and positive electrodes recorded at 1 mV s^{-1} in a three-electrode cell for the AC/TMBQ (3) (negative)||AC/PBQ (3) (positive) coin cells after cycle tests. The cycle tests were conducted (a) immediate after cell assembly, (b) after four CV cycles (1 mV s^{-1}, 0–0.8 V), and (c) after four GCD cycles (0.1 A g^{-1}, 0–0.8 V).

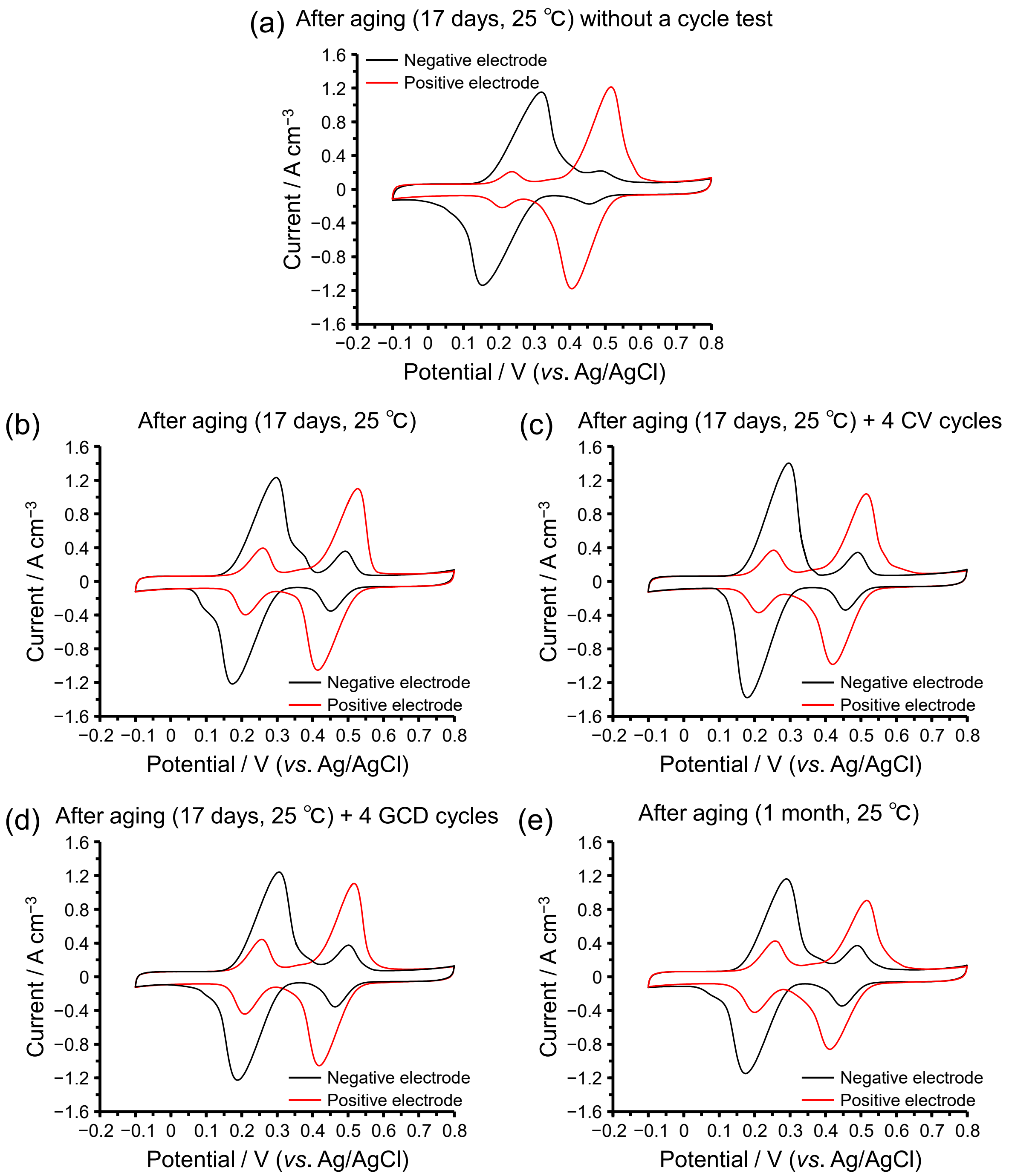

Fig. S27 Cyclic voltammograms of the negative and positive electrodes recorded at 1 mV s^{-1} in a three-electrode cell for the AC/TMBQ(3) (negative)||AC/PBQ(3) (positive) coin cells after aging and/or cycle tests. (a) Electrodes measured after aging at 25 °C for 17 days without prior cycling. The cycle tests prior to CV measurements in (b–e) were conducted as follows: (b) after aging (17 days, 25 °C), (c) after aging (17 days, 25 °C) followed by 4 CV cycles (1 mV s^{-1}, 0–0.8 V), (d) after aging (17 days, 25 °C) followed by 4 GCD cycles (0.1 A g^{-1}, 0–0.8 V), and (e) after aging (1 month, 25 °C).

Table S2 Distribution of TMBQ and PBQ species in the negative and positive electrodes of the AC/TMBQ (3)||AC/PBQ (3) coin cell under different cycling and aging conditions

	Utilization efficiencies			
	Negative electrode		Positive electrode	
Conditions	TMBQ [a]	PBQ [b]	TMBQ [c]	PBQ [d]
i [e]	90%	9%	5%	72%
ii [f]	86%	12%	10%	70%
iii [g]	86%	11%	10%	69%
iv [h]	80%	11%	14%	60%
v [i]	82%	10%	14%	61%
vi [j]	82%	12%	17%	61%
vii [k]	77%	13%	17%	55%
viii [l]	88%	4%	6%	74%

[a] TMBQ remaining in the negative electrodes.

[b] PBQ desorbed from the positive electrodes and subsequently adsorbed onto the negative electrodes.

[c] TMBQ desorbed from the negative electrodes and subsequently adsorbed onto the positive electrodes.

[d] PBQ remaining in the positive electrodes.

[e] Measured after the cycle test without prior treatment.

[f] Measured after four CV cycles (1 mV s^{-1}, 0–0.8 V) prior to the cycle test.

[g] Measured after four GCD cycles (0.1 A g^{-1}, 0–0.8 V) prior to the cycle test.

[h] Measured after aging for 17 days at 25 °C prior to the cycle test.

[i] Measured after aging for 17 days at 25 °C followed by four CV cycles (1 mV s^{-1}, 0–0.8 V) prior to the cycle test.

[j] Measured after aging for 17 days at 25 °C followed by four GCD cycles (0.1 A g^{-1}, 0–0.8 V) prior to the cycle test.

[k] Measured after aging for 1 month at 25 °C prior to the cycle test.

[l] Measured after aging for 17 days at 25 °C without subsequent cycling.

S27. Scalability evaluation of AC/TMBQ (3) hybrid preparation

To evaluate batch-scale feasibility, a tenfold scale-up experiment was conducted by increasing the amount of activated carbon from 100 mg to 1.0 g while keeping the QD loading (mmol g^{-1}) and mixing conditions unchanged. A 50 mL screw-cap vial was used for the mixing process. As shown in Fig. S28, complete adsorption was achieved and the electrochemical performance remained comparable to that of the laboratory-scale samples, indicating that the hybridization process is not limited to small batch sizes.

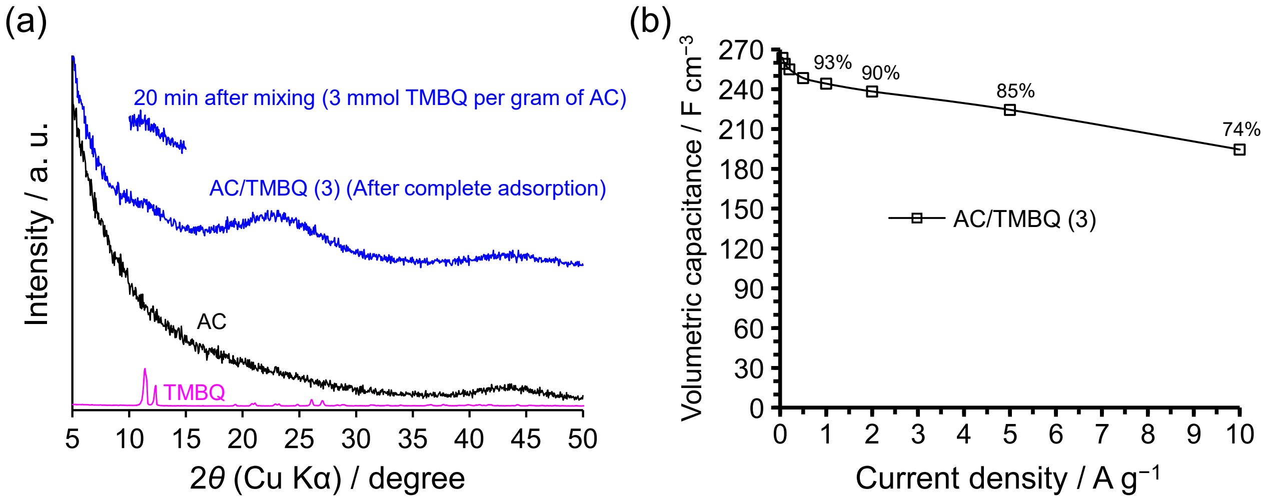

Fig. S28. Examination of the scalability of AC/TMBQ (3) preparation using a 1 g batch of AC in a 50 mL screw-cap vial: (a) XRD patterns of AC, TMBQ, the AC–TMBQ mixture collected 20 min after mixing, and AC/TMBQ (3) (after complete adsorption); (b) volumetric capacitance as a function of current density. The electrochemical measurements were performed in a three-electrode cell under the same conditions as those used in Fig. 5.